Title

Unsupervised segmentation of polarimetric SAR data using the covariance matrix

Journal

IEEE Transactions on Geoscience and Remote Sensing, 30(4)

ISSN

0196-2892

Authors

Rignot, E
Chellappa, R
Dubois, P

Publication Date

1992-07-01

DOI

10.1109/36.158863

Unsupervised Segmentation of Polarimetric SAR Data Using the Covariance Matrix

Eric Rignot, *Member, IEEE*, Rama Chellappa, *Fellow, IEEE*, and Pascale Dubois, *Member, IEEE*

Abstract— **This paper presents a method for unsupervised segmentation of polarimetric synthetic aperture radar (SAR) data into classes of homogeneous microwave polarimetric backscatter characteristics. Classes of polarimetric backscatter are selected based on a multidimensional fuzzy clustering of the logarithm of the parameters composing the polarimetric covariance matrix. The clustering procedure uses both polarimetric amplitude and phase information, is adapted to the presence of image speckle, and does not require an arbitrary weighting of the different polarimetric channels; it also provides a partitioning of each data sample used for clustering into multiple clusters. Given the classes of polarimetric backscatter, the entire image is classified using a Maximum A Posteriori polarimetric classifier. Four-look polarimetric SAR complex data of lava flows and of sea ice acquired by the NASA/JPL airborne polarimetric radar (AIRSAR) are segmented using this technique. The results are discussed and compared with those obtained using supervised techniques.**

I. Introduction

A number of polarimetric SAR analysis techniques have been reported in the literature to measure and characterize the polarization response of natural targets [1], to maximize the contrast between regions based on polarimetric filtering [2], or to classify data using Bayes' classifier [3]-[7]. Most of these techniques are supervised and require selection of training areas for each class of terrain cover. The process is precise, reliable, and only is concerned about the classes of interest to the user. However, an accurate and detailed knowledge of the scene contents is required to select the appropriate classes, and training areas should be homogeneous and contain enough samples to estimate the polarimetric backscatter characteristics of each class with good accuracy. This is not always possible, e.g., in the case of sea ice studies where ground truth data are often sparse and time-limited (due to the cost of collecting extensive ground truth information and the rapid evolution of the ice), and sea ice features are difficult to characterize and extract (e.g., ridges, broken-up ice floes, and open leads). In addition, selecting training areas becomes costly and time consuming as the number of classes, the data volume, and the data rate increase.

Manuscript received September 12, 1991; revised February 16, 1992. This work was carried out under contract with the National Aeronautics and Space Administration at the Jet Propulsion Laboratory, California Institute of Technology.

E. Rignot and P. Dubois are with the Jet Propulsion Laboratory, California Institute of Technology, Pasadena, CA 91109.

R. Chellappa is with the Department of Electrical Engineering, Institute for Advanced Computer Studies and Center for Automation Research, University of Maryland, College Park, MD 20742.

IEEE Log Number 9200970.

Because of these limitations, there is a strong interest in developing unsupervised techniques analyzing polarimetric SAR data. Although the physical interpretation of the results can be more difficult, unsupervised techniques are complementary to supervised techniques and also significantly decrease the operator–system interactions, an important advantage for the development of automatic and real-time classifiers for SAR data. One unsupervised technique was described in [8], which automatically classifies polarimetric SAR data into four categories of dominant scattering mechanisms: 1) single bounce scattering; 2) double bounce scattering; 3) diffuse or multiple bounce scattering; 4) nonclassified scattering. The results have a direct physical interpretability and greatly help to characterize the interactions between the electromagnetic signal and the natural media. In cases where the same type of scattering mechanism dominates the entire scene, however, that particular technique does not help to separate different types of natural surfaces. In this paper, a more discriminative method of unsupervised analysis for polarimetric SAR data is presented which segments the data into classes of homogeneous microwave polarimetric backscatter characteristics. Classes of polarimetric backscatter are selected based on a multidimensional fuzzy clustering of the logarithm of the parameters composing the polarimetric covariance matrix. The advantages of operating in the log domain are outlined in the paper. The degree of discriminability of the cluster centers is fixed by three required user-input clustering parameters. These parameters are: 1) the expected number of clusters; 2) the minimum separation between cluster centers, and 3) the maximum size of each cluster. Given the classes of polarimetric backscatter, a Maximum A Posteriori (MAP) polarimetric classifier described in [7] is used to segment the entire polarimetric array. The potential and usefulness of the unsupervised technique is illustrated using fully polarimetric SAR complex data acquired by the NASA/Jet Propulsion Laboratory airborne polarimetric radar (AIRSAR). The segmentation results are compared to those obtained from scattering mechanisms [8] and the supervised classification based on training areas [3]-[7].

The paper is organized as follows. In Section II, the polarimetric feature vector used for clustering of the polarimetric SAR data and the clustering technique are defined. Section III briefly introduces the MAP polarimetric classifier, more details being available in [7]. Section IV presents the segmentation results obtained using AIRSAR polarimetric data and compares them with those obtained from other techniques. Section V concludes the paper.

II. Selection of the Image Classes

In this section, the process of unsupervised selection of the classes of polarimetric backscatter is described. A clustering technique is used to make the selection. The process involves only a small percentage of data samples picked blindly across the whole image from a regular grid. Using more than 10% data samples would increase the computational cost of clustering without significantly improving the estimation accuracy of the cluster centers [9]. Section III describes how to subsequently classify the entire image.

Let $\boldsymbol{X}_s$ denote the polarimetric vector of the complex measurements at pixel site s

$$\boldsymbol{X}_s = [\mathrm{HH}, \mathrm{HV}, \mathrm{VV}]_s \tag{1}$$

where, for instance,

$$\mathrm{HV} = \mid \mathrm{HV} \mid exp\,\{i\,\phi_{\mathrm{HV}}\}. \tag{2}$$

HV is the complex amplitude of the V- (vertical) polarized return given that the transmitted signal is H- (horizontal) polarized. $\mid \mathrm{HV} \mid$ denotes its amplitude and ϕ_{HV} its phase. The complex amplitude VH, also acquired by the SAR receiver, is not present in (1) as VH and HV are symmetrized during compression and calibration of the polarimetric SAR data based on the reciprocity principle [10].

In the absence of a textural modulation of the backscatter coefficient of the surface, the polarimetric measurement vector $\boldsymbol{X}_s$ is multivariate Gaussian [4]. The conditional distribution of $\boldsymbol{X}_s$ given its class label $L_s = l$, with $l \in \{1, \ldots, K\}$ where K is the number of classes in the image, is

$$p\,(\boldsymbol{X}_s \,/\, L_s = l) = \frac{1}{\pi^3 \mid \boldsymbol{C}_l \mid} exp\,\{-\boldsymbol{X}_s^*\, \boldsymbol{C}_l^{-1}\, \boldsymbol{X}_s^T\} \tag{3}$$

where the superscript $*$ denotes complex conjugation, the superscript T denotes transposition, and $< >$ denotes ensemble averaging. The matrix $\boldsymbol{C}_l = < \boldsymbol{X}^{*T} \boldsymbol{X} >_l$ is the polarimetric covariance matrix of the data in region l. For azimuthally symmetric targets (see [11] for a discussion), applicable to a large number of natural surfaces, HV is uncorrelated with HH and VV [12], and the Hermitian matrix $\boldsymbol{C}_l$ has four zero elements

$$\boldsymbol{C}_l = \begin{pmatrix} <\mid \mathrm{HH} \mid^2> & 0 & < \mathrm{HHVV}^* > \\ 0 & <\mid \mathrm{HV} \mid^2> & 0 \\ < \mathrm{HH}^* \mathrm{VV} > & 0 & <\mid \mathrm{VV} \mid^2> \end{pmatrix} \tag{4}$$

The polarimetric covariance matrix $\boldsymbol{C}_l$ completely characterizes the first order statistical characteristics of class l of polarimetric backscatter (3). Hence, a possible mode of unsupervised selection of the classes of polarimetric backscatter is to perform clustering on a feature vector that comprises all the parameters composing the matrix $\boldsymbol{C}_l$. We choose the feature vector $\boldsymbol{x}_C$ to be equal to ten times the logarithm of the parameters composing the polarimetric covariance matrix as

$$\boldsymbol{x}_C = \begin{pmatrix} 10\ \log_{10}(<\mid \mathrm{HH} \mid^2>) \\ 10\ \log_{10}(<\mid \mathrm{HV} \mid^2>) \\ 10\ \log_{10}(<\mid \mathrm{VV} \mid^2>) \\ 10\ \log_{10}(\mid < \mathrm{HHVV}^* > \mid) \\ 10\ \frac{arg < \mathrm{HHVV}^* >}{\log(10.)} \end{pmatrix} \tag{5}$$

where arg denotes the argument of a complex number. The first three coefficients represent the backscatter cross sections in dB of the surface element at three different linear polarizations. The fourth and fifth components correspond respectively to the real and imaginary parts of the logarithm of the $< \mathrm{HHVV}^* >$ cross product multiplied by ten. The fourth component measures the magnitude of the HH–VV correlation function, and the fifth one is proportional to the HH–VV phase difference. The first four elements have typically a dynamic range of about 30 dB, and the fifth one of 27.2 dB as $\phi_{\mathrm{HHVV}} \in [-\pi, +\pi]$. The polarimetric feature vector $\boldsymbol{x}_C$ contains the complete polarimetric amplitude and phase information in the case of azimuthally symmetric targets.

The advantages of operating in the log domain instead of the linear domain are two-fold:

1. Traditional clustering techniques are mainly driven by the amplitude variance of the signal. In SAR data, because of image speckle, the amplitude variance is proportional to its mean for magnitude-squared detection. As a result, more clusters are selected in the high backscatter regions than in the low backscatter regions, as noted in [13]. In the log domain, however, image speckle has the statistical characteristics of additive noise with the power level not varying much across the image, and therefore does not impair the selection of cluster centers across the dynamic range of backscatter. Operating in the log domain therefore renders clustering robust to the presence of image speckle.
2. In the linear domain, the cross-polarized terms (i.e., HV) are often several orders of magnitude smaller than the copolarized terms (i.e., HH or VV), and clustering is mainly driven by the copolarized terms unless an arbitrary weighting of the different channels is used. The optimal weighting may vary with the type of target or the environmental conditions. In the log domain, the difference in backscatter between cluster centers is measured in dB, i.e., independent of the difference in absolute magnitude between each channel. Weighting of the different channels is not necessary.

Logarithmic scaling is commonly used to represent radar backscatter values as the dynamic range of SAR data is large. It is therefore advantageous to use the same unit in selecting the clustering parameters. Note here that the 0 dB reference values implicitly used in each component of $\boldsymbol{x}_C$ have no influence on clustering. It is only assumed that an "x" dB change in one component of $\boldsymbol{x}_C$ (e.g., HH) carries the same weight as an "x" dB change in another component (e.g., HV) which, in the absence of any knowledge of the usefulness of each polarimetric channel in separating different types of natural targets, is a reasonable assumption.

In the presence of nonazimuthally symmetric natural targets, the polarimetric feature vector $\boldsymbol{x}_C$ must include four additional components. We did not investigate the usefulness of these additional components in our polarimetric data set. The AIRSAR data have been calibrated using the procedure described in [11] which assumes azimuthal symmetry of at least one large distributed target and which produces calibrated images

where these four additional components are below the system noise level over the entire scene.

To measure the separation between a polarimetric feature vector $\boldsymbol{x}_{C,i}$ of the i^{th} sample and a cluster center $\boldsymbol{C}_l$ (written as a vector similar to $\boldsymbol{x}_C$), an Euclidean distance may be used. The choice of this metric leads to the iterated k-means or ISODATA clustering algorithm [14] which minimizes the functional

$$E_1 = \sum_{l=1}^{l=K} \{ \sum_{i=1}^{i=M} \delta_k(L_i - l) \, |\boldsymbol{x}_{\boldsymbol{C},i} - \boldsymbol{C}_l|^2 \} \tag{6}$$

where δ_k is the Kronecker delta (i.e. $\delta_k(L_i - l)$ is one if $L_i = l$, and zero otherwise). The cluster centers are determined from the iterated sample means. In addition, ISODATA uses heuristics and a number of input parameters to split or lump clusters. It provides information about the degree of homogeneity and separation of individual clusters via the size of each cluster and the distance between cluster centers. Yet, each sample used for clustering is assumed to be perfectly homogeneous and to belong to only one cluster. In many real images, sample areas may contain a mixture distribution of various classes. This could be due to the limited spatial resolution of the polarimetric imager or to the scene inhomogeneity. To account for the partitioning of each sample element $\boldsymbol{x}_{C,i}$ into several clusters $\boldsymbol{C}_l$, instead of (6), the following objective function is used

$$E_m = \sum_{l=1}^{l=K} \sum_{i=1}^{i=M} p \, (\boldsymbol{x}_{C,i} \, , \, L_i = l)^m \mid \boldsymbol{x}_{C,i} - \boldsymbol{C}_l \mid^2 \tag{7}$$

where M is the number of sample points used for clustering (typically a few percentages of the total number of pixel elements in the image), m is a positive constant greater than one, and p is the partition function or probability of sample $\boldsymbol{x}_{C,i}$ to belong to cluster l. ISODATA corresponds to the case where p is a hard partition (i.e., p is equal to one when $\boldsymbol{x}_{C,i}$ belongs to cluster l, and zero otherwise), and $m = 1$. The minimization of the objective function E_m corresponds to the fuzzy c-means algorithm [15], [16] and is achieved using

$$p \, (\boldsymbol{x}_{C,i}, \, L_i = l) = (\sum_{j=1}^{j=K} \frac{\mid \boldsymbol{x}_{C,i} - \boldsymbol{C}_l \mid^2}{\mid \boldsymbol{x}_{C,i} - \boldsymbol{C}_j \mid^2})^{-1/(m-1)} \tag{8}$$

and

$$\boldsymbol{C}_j = \frac{\sum_{i=1}^{i=M} p \, (\boldsymbol{x}_{C,i} \, , \, j) \, \boldsymbol{x}_{C,i}}{\sum_{i=1}^{i=M} p \, (\boldsymbol{x}_{C,i} \, , \, j)} \tag{9}$$

in an iterative convergent process [16], [17]. In our experiments, $m = 1.4$, the initial configuration of the cluster centers is the ISODATA solution, and the fuzzy c-means optimization process is iterated until the number of sample points that change their partition function p by more than $\epsilon = 0.01$ is less than 4%.

Most of the required user-input clustering parameters are not scene dependent, except the expected number of clusters, the minimum separation between cluster centers, and the maximum size of each cluster. These three parameters fix the degree of discriminability of the different classes. In that aspect, the method is never completely unsupervised. In some cases, the expected number of classes may be known in advance. For example, at the Alaska SAR Facility, the Geophysical Processor System must classify spaceborne SAR data of sea ice into four categories [18]: 1) *multiyear sea ice*; 2) *first year sea ice*; 3) *thin ice*; and 4) *open water*. Otherwise, the number of classes is limited by the finite dynamic range of the polarimetric measurements and the minimum separability between clusters. In our experiments, good results are obtained when the polarimetric distance between cluster centers is at least 3 dB and the size of each cluster is less than 3 dB. The radiometric fidelity of the image (typically 1 dB) and the inherent variability of the polarimetric characteristics of each area with the incidence angle (typically 1–3 dB) set limits on the minimum separability between clusters.

The danger of operating in the log-domain is that logarithmically transformed cross-section and cross-product values have different statistics [19]. As a result, conversion of the characteristics of the cluster centers from a dB scale back to a linear scale must be done carefully. When the equivalent number of looks of the iterated sample means is high enough, a direct conversion is possible as the bias introduced by the logarithmic transformation will be small [19].

Finally, a known inconvenience of the fuzzy c-means/ ISODATA clustering algorithm is that it is not adapted to the situation where natural clusters are elongated in one direction. In the case of polarimetric SAR data, at a given incidence angle, the variability of the cluster elements can be modeled as resulting from three different sources: 1) image speckle; 2) system noise; and 3) texture [20]. In the log-domain, the variance of the signal due to image speckle and system noise is the same at all polarizations (system noise, however, biases the value of the cluster centers and affects their separability at low signal-to-noise ratios (SNR's)). Furthermore, in all the four-look AIRSAR data used in this study, the variance of texture was always found to be small in magnitude compared to the intracluster distances and not varying much with polarization. As a result, it is reasonable to assume that the clusters are nearly spherical in the polarimetric feature space.

III. MAP Polarimetric Classifier

In Section II, we showed how to determine the polarimetric cluster centers of the image from a small subset of the data samples. In this section, we describe how a MAP classifier [7] is used to classify the entire image given the cluster centers.

A model of the conditional distribution of the polarimetric data samples (3) is combined with a Markov random field representing the distribution of the class labels L_s to obtain an expression for the posterior distribution of the class labels given the polarimetric SAR observations [7]. In a Bayesian framework, the most likely class labeling of the data is the one which maximizes the posterior distribution of the class labels and is called the MAP estimate.

The computation of the MAP solution is more demanding than that of the Maximum Likelihood (ML) solution described in [3], but new computational techniques have been developed recently to speed up the estimation process [7].

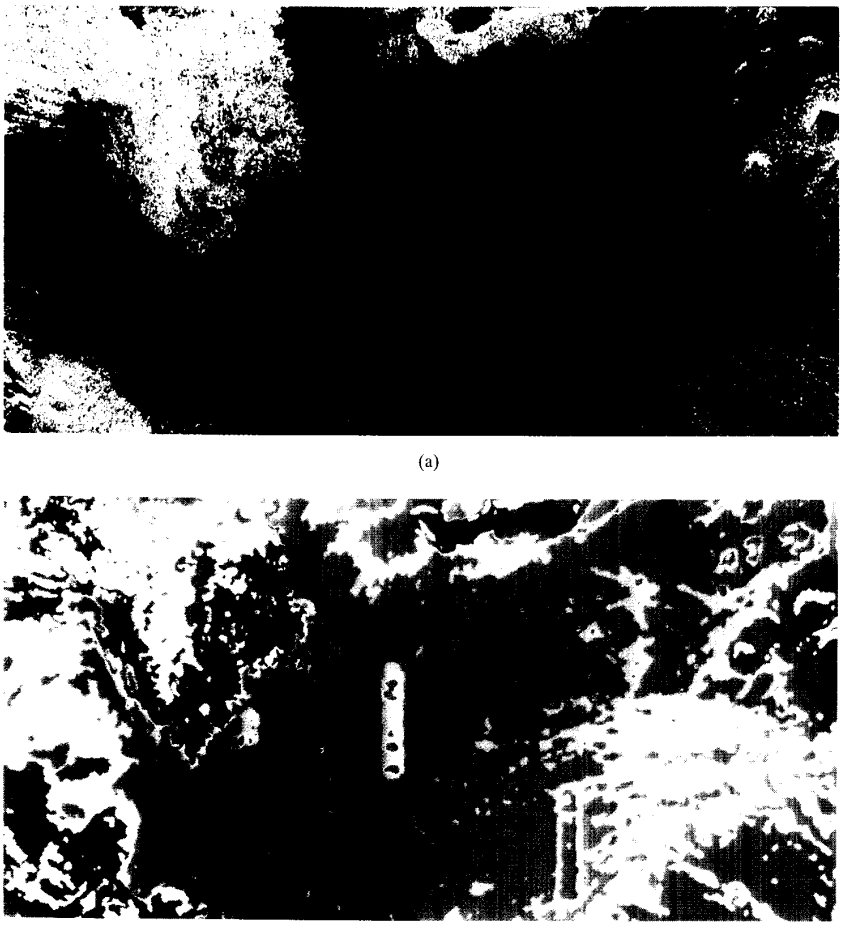

Fig. 1. (a) Color overlay at three polarizations (HH is red, VV is green, and HV is blue) and L-band frequency of a four-look AIRSAR image of the Pisgah lava flows in the Mojave Desert, CA. The image is in slant-range and covers a 12 km×5 km area. The incidence angle varies between 38° (top in the figure) and 53° (bottom in the figure). (b) Unsupervised MAP segmentation map of Fig. 1(a) using six classes and the complete polarimetry. Class one (phase II lava) is colored white, class two (phase III lava) is colored brown, class three (phase I lava) is colored red, class four (alluvial fan and cobble) is colored light green, class five (alluvial fan) is colored dark green, and class six (dry lake bed) is colored dark blue.

Results obtained using AIRSAR polarimetric SAR complex data indicate that the MAP classifier improves classification accuracy by 10–20 percentage points compared to the ML classifier which assumes equal *a priori* probabilities for the classes and no spatial correlation between the polarimetric measurements.

IV. Results Using AIRSAR Data

A. Images of Lava Flows

Fig. 1(a) shows a color overlay at L-band frequency ($\lambda = 23.98$ cm) and three different polarizations (HH is red, VV is green, and HV is blue) of a four-look AIRSAR image of the Pisgah lava flows in the Mojave Desert, CA [21]. In this figure, near range is on top and the aircraft is flying from right to left. The image is 1024 pixels by 512 records in size. The incidence angle varies between 38 and 53°. The original image has 750 records. The first records of the data take, corresponding to smaller incidence angles, are not used as they correspond to a portion of the image where the incidence angle effects on the backscatter characteristics of the SAR data cannot be ignored as they would cause significant variations within each intended cluster. Pixel spacing is 12.1 m in azimuth and 6.66 m in slant-range. The data have been calibrated using the procedure for polarimetric SAR data described in [11]. The scene contains various geological surfaces [13], [21], [22], which can be divided into six classes of terrain cover: phase I lava, phase II lava, phase III lava, cobble, alluvial surface, and dry lake bed. Table I lists the polarimetric backscatter characteristics of these six classes based on the selection of six training areas.

A set of 101×51 polarimetric data samples were clustered into six classes separated by more than 4 dB. The polarimetric characteristics of the resulting cluster centers are given in Table II. All clusters have a good degree of homogeneity as the variance of their elements is less than 1 dB (not shown in Table II), and are well separated as the distance

TABLE I
POLARIMETRIC CHARACTERISTICS OF THE SIX TRAINING AREAS OF THE PISGAH SCENE AT *L*-BAND

Training Area	σ_{HH} (dB)	σ_{HV} (dB)	σ_{VV} (dB)	σ_{HHVV} (dB)	ϕ_{HHVV} (rad)
Phase II lava	-8.0	-17.7	-8.5	-9.8	0.0
Phase III lava	-9.5	-22.2	-10.2	-10.7	0.0
Phase I lava	-16.0	-26.9	-15.3	-16.9	-0.2
Cobble	-19.0	-31.7	-17.8	-19.2	-0.4
Alluvial fan	-23.8	-34.4	-22.8	-24.7	-0.0
Dry Lake Bed	-29.2	-41.6	-28.0	-29.6	-0.1

TABLE II
POLARIMETRIC CHARACTERISTICS OF THE SIX CLUSTER CENTERS OF THE PISGAH SCENE AT *L*-BAND

Cluster Number	σ_{HH} (dB)	σ_{HV} (dB)	σ_{VV} (dB)	σ_{HHVV} (dB)	ϕ_{HHVV} (rad)	Target Type
1	-8.9	-19.4	-9.4	-10.4	0.0	Phase II lava
2	-13.2	-24.2	-13.2	-14.5	0.1	Phase III lava
3	-17.7	-29.1	-17.1	-18.6	0.2	Phase I lava
4	-20.9	-32.7	-20.1	-21.7	0.1	Alluvial fan 1
5	-23.7	-36.3	-22.9	-24.4	0.0	Alluvial fan 2
6	-28.3	-41.0	-27.0	-28.8	0.1	Dry lake bed

between cluster centers is more than 4 dB. Clustering appears to be mainly driven by the radiometric information contained in the first three components of $\boldsymbol{x}_C$. In effect, the HH-VV phase difference is zero almost everywhere in the image and does not help to separate the different types of terrain cover. The fourth component of $\boldsymbol{x}_C$ corresponds to a HH-VV correlation coefficient (i.e., $| \rho_{HHVV} | = \frac{|<HHVV^*>|}{\sqrt{<|HH|^2><|VV|^2>}}$) between 0.7 and 0.8 for all cluster centers, which indicates little discriminability between the natural surfaces for this parameter. By comparing Tables I and II, one sees that the backscatter characteristics of the cluster centers are consistent with the backscatter characteristics of the different types of terrain obtained from training areas. Note that the cobble site is classified in the same cluster as the alluvial surface, as expected, since they have similar polarimetric backscatter characteristics at *L*-band frequency (Table I).

The unsupervised MAP classification map is shown in Fig. 1(b). There is a good agreement between this map and the geological map [22] or the supervised classification map in [10]. However, in both the supervised and unsupervised maps, topography causes some misclassification in the near-range (top of the figure). This problem is characteristic of the sensitivity of SAR data to relief and illustrates that for any classifier to work in a mountainous area the incidence angle effect must be included. The division of the alluvial surface into two image classes in Fig. 1(b) is also due to the presence of relief.

Unsupervised classification by scattering mechanisms [8] shows that the dominant form of scattering is single bounce over the entire image except in the two areas corrupted by interferences with unknown sources (rectangular patterns colored in pink in the bottom center of Fig. 1(a)). Hence, this type of classification scheme does not separate the different types of terrain in this example at *L*-band frequency.

B. Images of Sea Ice

Fig. 2(a) shows a color overlay at *L*-band frequency and three polarizations (HH is red, VV is green, and HV is blue) of a four-look AIRSAR image of sea ice acquired in the winter season over the Beaufort Sea, Alaska. The incidence angle varies between 37 and 52 °. The data have been relatively calibrated using the procedure described in [11] but could not be absolutely calibrated due to the absence of targets of known backscatter characteristics in the scene. An arbitrary gain factor was applied to obtain reasonable values of the backscatter cross-section of multiyear sea ice at *L*-band HH-polarization based on past scatterometer measurements.

A visual inspection of the SAR data reveals that at least five different types of sea ice are present in the imagery: 1) *multiyear sea ice* (abreviated MY), an old ice that survived one or more summer melts, several meters thick, and which corresponds to large ice floes of rounded and smooth geometrical shape in Fig. 2(a); 2) *first year smooth ice* (abreviated FYS), about 1 m thick, with a smooth surface, which appears dark in Fig. 2(a) and constitutes the matrix of the MY ice floes; 3) *first year rough* (abbreviated FYR), less than a meter thick, with a rough surface and many ridges, which appears brighter than FYS ice in Fig. 2(a); 4) *ridges*, resulting from the continuous action of shear and compressing forces between sea ice floes, and which appear dominantly bright in Fig. 2(a); 5) *thin ice* (abreviated ThI), which appears the darkest in Fig. 2(a).

A set of 101 x 51 polarimetric data samples were clustered into eight classes separated by more than 3 dB. The polarimetric characteristics of the resulting cluster centers are shown in Table III. The corresponding MAP segmentation map is shown on Fig. 2(b). The first cluster corresponds to compressed FY surrounding MY floes and MY ridges within the MY ice floes. The next three clusters correspond to three different categories of FY ridge and rubble. Cluster five corresponds

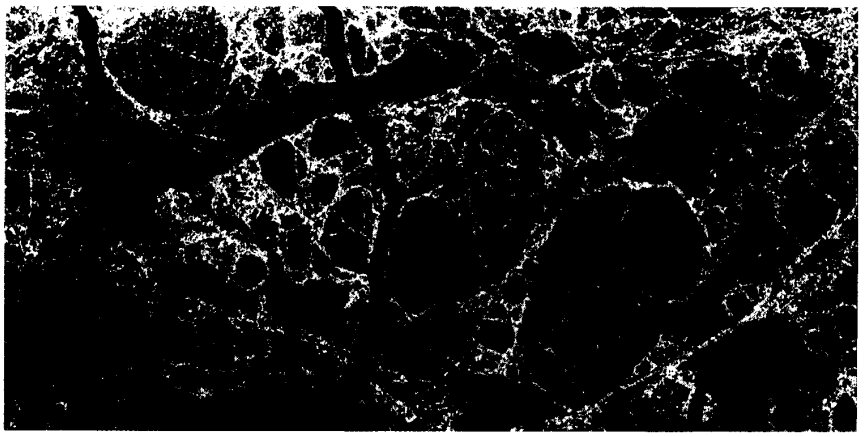

(a)

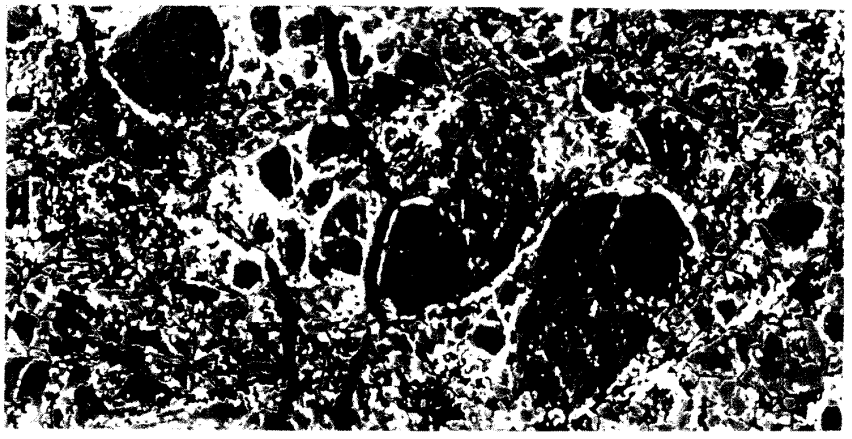

(b)

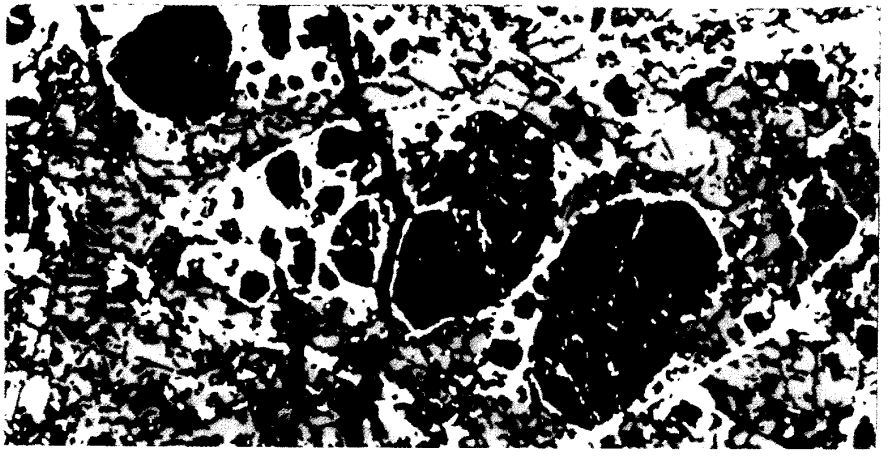

(c)

Fig. 2. (a) Color overlay at three polarizations (HH is red, VV is green, and HV is blue) and L-band frequency of a four-look AIRSAR image of sea ice from the Beaufort Sea, Alaska. The image is in slant-range and covers a 12 km$\times$5 km area. The incidence angle varies between 37° (top in the figure) and 52° (bottom in the figure). (b) Unsupervised MAP segmentation map of Fig. 2(a) using eight classes and the complete polarimetry. Class one (MY ridges and compressed FY) is colored white, class two (FY ridges I) is colored dark red, class three (FY ridges III) is colored orange, class four (FY ridges III) is colored yellow, class five (MY) is colored light blue, class six (FYR) is colored dark green, class seven (FYS) is colored dark blue, and class eight (ThI) is colored black. c) Unsupervised MAP segmentation of Fig. 2(a) using five classes and HH-polarization. Class one (MY and FY ridges) is colored white, class two (MY and FY ridges) is colored light blue, class three (MY and FY ridges) is colored dark blue, class four (FY) is colored green, and class five (ThI) is colored black.

TABLE III
POLARIMETRIC CHARACTERISTICS OF THE EIGHT CLUSTER CENTERS OF THE BEAUFORT SEA SCENE AT *L*-BAND

Cluster Number	σ_{HH} (dB)	σ_{HV} (dB)	σ_{VV} (dB)	σ_{HHVV} (dB)	ϕ_{HHVV} (rad)	Target Type
1	-12.4	-20.7	-8.8	-12.0	0.0	MY ridges + Compressed FY
2	-15.0	-24.7	-11.4	-14.4	0.0	FY ridge/rubble I
3	-17.2	-28.0	-13.5	-16.4	0.0	FY ridge/rubble II
4	-19.7	-30.5	-15.9	-19.0	-0.1	FY ridge/rubble III
5	-19.7	-34.0	-15.3	-17.9	0.0	MY
6	-23.0	-34.0	-19.0	-22.2	-0.1	FYR
7	-27.0	-40.0	-22.6	-26.2	-0.1	FYS
8	-34.0	-40.0	-28.0	-33.0	0.0	ThI

to the MY ice floes. The boundaries of the MY ice floes are clearly distinguishable in Fig. 2(b). Cluster six, seven, and eight correspond to FYR, FYS, and ThI, respectively.

In Table III, clusters four and five have the same HH and VV backscatter characteristics which indicates that MY and FY ridges (which correspond to different sea ice conditions) cannot be separated using the HH or VV amplitude alone at *L*-band frequency. An example is given in Fig. 2(c), where the data have been segmented using only the HH-polarization information and ridges within the FY ice are systematically misclassified as MY (colored light blue in Fig. 2(c)). Table III indicates that the parameters providing the best separability between clusters four (ridges) and five (MY) are HV, and, at a lesser degree, the correlation coefficient $|\rho_{HHVV}|$ between HH and VV. A higher HV return and a lower value of $|\rho_{HHVV}|$ in ridged ice compared to MY ice indicates a larger variability in orientation of the scatterers in ridged ice, a fact consistent with the more complex geometrical shape of the surface. Although HV offers a large contrast between cluster four and five, it does not separate cluster five and six, which indicates that MY and FYR cannot be well separated using the HV amplitude alone at *L*-band frequency. Similarly, cluster seven and eight have the same HV return, which is consistent with the fact that both surfaces (FYS and ThI) are smooth and are not expected to yield a significant amount of cross-polarized return. These results indicate that polarimetry significantly improves the capability of the radar imager to separate different sea ice conditions at *L*-band frequency. Small residual ambiguities are still visible in Fig. 2(b) as ridges within FY sea ice patches are sometimes misclassified as MY sea ice. These ambiguities are resolved when the *L*-band polarimetry is combined with the *C*-band polarimetry as shown in [9]. As in the previous example, the HH–VV phase difference is zero almost everywhere in the image and has no influence on the clustering results. Significant phase shifts between the HH and VV response have been detected when the electromagnetic wave double-bounces on the surface (e.g., man-made structures, tree-trunk/ground interaction in forested areas) as discussed in [8] but this was not the case of the examples studied in this work.

Interestingly, the use of the complete polarimetry renders the unsupervised segmentation technique more robust to changes in backscatter cross section with incidence angle for this example. MY ice floes in the top portion of Fig. 2(c) are not classified in the same cluster as MY ice floes in the middle and bottom portion of the image. The incidence angle effect is substantially reduced when the complete polarimetry is used in Fig. 2(b). One possible reason is that the HV return of the different sea ice types varies less with incidence angle than the HH and VV returns. Another reason is that, in general, the probability of error of the Bayes classifier decreases when the number of polarimetric channels increases as discussed in [3].

In the presence of ridges, it is very difficult to select homogeneous training areas containing enough sample elements. For that reason, it was not possible to obtain a segmentation map similar to Fig. 2(b) using supervised techniques. As discussed in the previous paragraphs, the clustering results also provide very useful information about the organization of the polarimetric feature space that would be difficult to obtain using supervised techniques.

Results from the unsupervised classification technique based on scattering mechanisms [8] show that the dominant form of scattering over the entire scene is single bounce. Again, in this particular example and at this frequency, this type of unsupervised classification does not help to separate different sea ice types.

V. CONCLUSION

The unsupervised segmentation technique for polarimetric SAR data presented in this paper uses both polarimetric amplitude and phase information, is adapted to the presence of image speckle, and requires minimal operator interventions. Its potential has been illustrated using polarimetric radar images from AIRSAR. The polarimetric clusters detected by the unsupervised technique are in good agreement with the natural classes present in the scene. In one example (sea ice), the clustering technique is found even more powerful than a supervised technique based on the selection of training areas. Further work is however needed to develop a technique which accounts for significant incidence angle effects, e.g., due to terrain or imaging geometry.

In future, SAR sensors will be capable of gathering a large volume of data at various polarizations and different frequencies. To analyze these data, it is desirable to developautomatic systems that require little or no operator supervision. We have presented in this paper a technique for unsupervised

segmentation of polarimetric SAR data. The next step in the automatic classification of polarimetric SAR data would be to automatically relate each cluster to characteric features of the natural target. This could be done using a look up table of the expected backscatter characteristics of natural targets. In the case of a single polarization radar system, the process has been implemented on an operational basis to classify sea ice types using SAR data acquired by the the European First Remote Sensing Satellite (E ERS-1) at the Alaska SAR Facility [18].

ACKNOWLEDGMENT

The authors would like to thank Jakob van Zyl and Ronald Kwok for their insightful comments, and the people from the AIRSAR team at the Jet Propulsion Laboratory who operated the imaging polarimeter and processed the data.

REFERENCES

[1] H. A. Zebker, J. J. van Zyl, and D. Held, "Imaging radar polarimetry from wave synthesis," *J. Geophys. Res.*, vol. 92, no. B1, pp. 683-701, Jan. 1987.

[2] A. A. Swartz, H. A. Yueh, J. A. Kong, L. M. Novak, and R. T. Shin, "Optimal polarizations for achieving maximum contrast in radar images," *J. Geophys. Res.*, vol. 93, no. B12, pp. 15, 252-15, 260, Dec. 1988.

[3] J. A. Kong, A. A. Swartz, H. A. Yueh, L. M. Novak, and R. T. Shin, "Identification of terrain cover using the optimum polarimetric classifier," *J. Electromagn. Waves and Applic.*, vol. 2, no. 2, pp. 171-194, 1988.

[4] S. H. Yueh, A. A. Swartz, J. A. Kong, R. T. Shin, and L. M. Novak, Bayes classification of terrain cover using normalized polarimetric data, "*J. Geophys. Res.*, vol. 93, no. B12, pp. 15, 261-15, 267, Dec. 1988

[5] H. H. Lim, A. A. Swartz, H. A. Yueh, J. A. Kong, R. T. Shin, and J. J. van Zyl, "Classification of Earth terrain using polarimetric synthetic aperture radar images," *J. Geophys. Res.*, vol. 94, pp. 7049-7057, June 1989.

[6] J. J. van Zyl and C. F. Burnette, "Bayesian classification of polarimetric SAR images using adaptive a-priori probabilities," *Int. J. Rem. Sens.*, in press, 1992.

[7] E. Rignot and R. Chellappa, "Segmentation of polarimetric synthetic aperture radar data," *IEEE Trans. Sig. Process.*, July 1992.

[8] J. J. van Zyl, "Unsupervised classification of scattering behavior using radar polarimetry data," *IEEE Trans. Geosci. Remote Sensing*, vol. 27, pp. 36-45, Jan. 1989.

[9] E. Rignot, "Segmentation of multifrequency and polarimetric synthetic aperture radar data," Ph.D. thesis, University of Southern California, Department of Electrical Engineering - Systems, May 1991.

[10] F. T. Ulaby and C. Elachi, Eds., *Radar Polarimetry for Geoscience Applications*. Norwood, MA: Artech House, 1990.

[11] J. J. van Zyl, "Calibration of polarimetric radar images using only image parameters and trihedral corner reflector responses," *IEEE Trans. Geosci. Remote Sensing*, vol. 28, pp. 337-348, May 1990.

[12] M. Borgeaud, R. T. Shin, and J. A. Kong, "Theoretical models for polarimetric radar clutter," *J. Electromagn. Waves and Applic.*, vol. 1, no. 1, pp. 67-86, 1987.

[13] C. F. Burnette, P. C. Dubois, and J. J. van Zyl, "Segmentation of multifrequency polarimetric radar images to facilitate the inference of geophysical parameters," *Proc. IEEE Int. Geosci. and Remote Sensing Symp.*, Vancouver, B. C., vol. 1, pp. 30-33, July 1989.

[14] G. H. Bell and D. J. Hall, "A clustering technique for summarizing multi-variate data," *Beh. Sci.*, vol. 12, pp. 153-155, 1974.

[15] J. C. Bezdek, *Pattern Recognition with fuzzy objective function algorithms*, Plenum, New York, 1981.

[16] J. C. Bezdek, R. Ehrlich, and W. Full, "FCM: The fuzzy c-means clustering algorithm," *Comp. Geosci.*, vol. 10, pp. 191-203, 1984.

[17] J. C. Bezdek, R. J. Hathaway, M. J. Sabin, and W. T. Tucker, "Convergence Theory for fuzzy c-means: counter-examples and repairs," *IEEE Trans. Syst., Man, Cybern.*, vol. SMC-17, pp. 873-877, 1987.

[18] R. Kwok, E. Rignot, B. Holt, and R. Onstott, "Identification of sea-ice types in spaceborne SAR data," *J. Geophys. Res.*, vol. 97, pp. 2391–2402, Feb. 1992.

[19] D. H. Hoekman, "Speckle ensemble statistics of logarithmically scaled data," *IEEE Trans. Geosci. Remote Sensing*, vol. 29, pp. 180-182, Jan. 1991.

[20] E. Rignot and R. Kwok, "Characterization of spatial statistics of distributed targets in SAR data," *Int. J. Remote Sensing*, in press, 1992.

[21] S. Wall, "The Mojave Field Experiment: Precursor to the Planetary Test Site," 20^{th} *Ann. Meet. of the Div. of Planet. Sci. of the Am. Astron. Soc.*, Austin, TX, Oct. 1985.

[22] W. S. Wise, "Geological map of the Pisgah and Sunshine cone lava fields," NASA TL-11, 8 pp., 1966.

Eric J. M. Rignot (M'91) was born in Chambon sur Lignon, France. He received the Engineer's diploma from the Ecole Centrale des Arts et Manufactures Paris in 1985, the M.S. degree in astronomy from the University of Paris VI in 1986, the M.S. degrees in aerospace engineering and electrical engineering in 1987 and 1988, respectively, and the Ph.D. degree in electrical engineering from the University of Southern California in 1991. His doctoral thesis was on the segmentation of multifrequency and polarimetric synthetic aperture radar data.

He was employed as a research assistant at the University of Southern California in the Department of Aerospace Engineering from 1986 to 1988. He then joined the Jet Propulsion Laboratory, California Institute of Technology, as a member of the technical staff in the Radar Science and Engineering section. His current interests include multisensor image registration, sea ice classification from spaceborne data, multifrequency radar polarimetry of glacier ice, and radar monitoring of environmental and phenologic changes in the boreal forests of Alaska.

Dr. Rignot is a Member of IEEE.

Rama Chellappa (S'78–M'79–S'79–M'81–SM'83–F'92) was born in Tanjore, Madras, India in 1953. He received the B.S. degree (with honors) in electronics and communication engineering from the Indian Institute of Science, Bangalore, in 1977. He received the M.S. and Ph.D. degrees in electrical engineering from Purdue University in 1978 and 1981, respectively.

From 1979 to 1981, Chellappa was a faculty research assistant at the Computer Vision Laboratory, University of Maryland. From 1981 to 1991, he was a faculty member in the Department of Electrical Engineering Systems, University of Southern California. From 1988 to 1990, he ws also Director of the Signal and Image Processing Institute at USC. Since August 1, 1991, he has been a professor in the Department of Electrical Engineering at the University of Maryland, where he is also affiliated with the Center for Automation Research, Computer Science Department and the Institute for Advanced Computer Studies. His current research interests are in signal and image procesing, computer vision, and pattern recognition. He was general chairman of the IEEE Computer Society Conference on Computer Vision and Pattern Recognition and of the IEEEE Computer Society Workshop on Artificial Intelligence for Computer Vision, both held in San Diego in June 1989. He was a program cochairman for the NSF sponsored Workshop on Markov Random Fields, which was also held in San Diego in June 1989.

Dr. Chellappa is coeditor of two volumes of selected papers on digital image processing and analysis published in 1985. He was an associate editor for the IEEE TRANSACTIONS ON ACOUSTICS, SPEECH, AND SIGNAL PROCESSING from 1987 to 1989. Currently, he is a coeditor-in-chief of *Computer Vision, Graphics, and Image Processing: Graphic Models and Image Processing* and is an associate editor for the IEEE TRANSACTIONS ON NEURAL NETWORKS and the IEEE TRANSACTIONS ON IMAGE PROCESSING. He has authored ten book chapters and over 100 journal and conference papers. Many of his papers have been reprinted in collected works published by IEEE Press, IEEE Computer Society Press, and MIT Press. He has supervised 16 doctoral dissertations. During the period from 1969 to 1975 Chellappa received a national scholarship from the Government of India , and he received the 1975 Jawaharlal Nehru Memorial Award from the Department of Education, Government of India. In addition, he received the 1985 National Science Foundation (NSF) Presidential Young Investigator Award and the 1985 IBM Faculty Development Award. In 1990 he received the Excellence in Teaching Award from the School of Engineering at USC.

Dr. Chellappa is a Fellow of IEEE.

Pascale C. Dubois (A'87) was born in Douera, Algeria. She received the Engineer's diploma from the Ecole Nationale Superieure de Constructions Aeronautics, Toulouse, France, in 1983. She received the Master's degree and the the Aeronautic Engineer's degree in 1984 and 1986, respectively, from the California Institute of Technology.

She then joined the Radar Science and Engineering section at the Jet Propulsion Laboratory. She has worked on the Magellan Project, the SIR-C project, and the AIRSAR system. Her current interests include science applications of SAR data to hydrology and geology as well as calibration of polarimetric SAR data as related to SIR-C.

Ms. Dubois is a Member of IEEE.